Oligomodal metamaterials with multifunctional mechanics

Aleksi Bossart[a,b,1], David M. J. Dykstra[a,1], Jop van der Laan[a], and Corentin Coulais[a,2]

[a]Institute of Physics, University of Amsterdam, 1098 XH Amsterdam, The Netherlands; and [b]Laboratory of Wave Engineering, École Polytechnique Fédérale de Lausanne, 1015 Lausanne, Switzerland

Edited by Katia Bertoldi, Harvard University, Cambridge, MA, and accepted by Editorial Board Member John A. Rogers April 2, 2021 (received for review September 9, 2020)

Mechanical metamaterials are artificial composites that exhibit a wide range of advanced functionalities such as negative Poisson's ratio, shape shifting, topological protection, multistability, extreme strength-to-density ratio, and enhanced energy dissipation. In particular, flexible metamaterials often harness zero-energy deformation modes. To date, such flexible metamaterials have a single property, for example, a single shape change, or are pluripotent, that is, they can have many different responses, but typically require complex actuation protocols. Here, we introduce a class of oligomodal metamaterials that encode a few distinct properties that can be selectively controlled under uniaxial compression. To demonstrate this concept, we introduce a combinatorial design space containing various families of metamaterials. These families include monomodal (i.e., with a single zero-energy deformation mode); oligomodal (i.e., with a constant number of zero-energy deformation modes); and plurimodal (i.e., with many zero-energy deformation modes), whose number increases with system size. We then confirm the multifunctional nature of oligomodal metamaterials using both boundary textures and viscoelasticity. In particular, we realize a metamaterial that has a negative (positive) Poisson's ratio for low (high) compression rate over a finite range of strains. The ability of our oligomodal metamaterials to host multiple mechanical responses within a single structure paves the way toward multifunctional materials and devices.

multifunctional | metamaterial | viscoelasticity | combinatorial

Flexible metamaterials use carefully designed arrangements of deformable building blocks to achieve unusual and tunable mechanical functionalities (1). Such mechanical responses rely on on-demand deformation pathways that cost a relatively low amount of elastic energy. A useful and widely applicable paradigm for the design of such pathways leverages the limit in which their elastic energy is zero—these pathways then become mechanisms or zero-energy modes. Flexible metamaterials based on such principle are, so far, either monomodal (Fig. 1*A*) or plurimodal (Fig. 1*C*). On one hand, monomodal metamaterials feature a single zero-energy mode and a single functionality (2–8), which is typically robust and easy to control with a simple actuation protocol, that is, a protocol that requires a single actuator, for example, uniaxial compression. On the other hand, plurimodal metamaterials feature a large number of zero-energy modes, which increases with system size (9, 10). The presence of these multiple zero modes offers multiple possible functionalities in principle, but they are hard to control in practice; that is, they require complex actuation protocols—protocols that require more than one actuator—for successful execution (9). The challenge we address here is whether it is possible to find a middle ground between monomodal and plurimodal metamaterials. In other words, can we design and create metamaterials that have more than one zero-energy mode, but not a number that grows with system size? For convenience and clarity, we term such metamaterials *oligomodal* (Fig. 1*B*). Could oligomodal metamaterials be actuated in a robust fashion with a simple actuation protocol (Fig. 1*B*)? Could oligomodal metamaterials host distinct mechanical properties within a single structure?

Combinatorial Analysis

To first design oligomodal architectures, we turn toward combinatorial metamaterials, which is a particularly fruitful paradigm for the design of advanced mechanical functionalities (4, 11, 12). In combinatorial metamaterials, the structural complexity is reduced to a discrete design space, typically, by controlling the orientation of the constitutive unit cells. Such discreteness makes the design space much easier to explore and has recently been leveraged to create nonperiodic metamaterials with shape-changing (4, 11) and topological properties (12), yet only for single zero-energy mode metamaterials so far. Here, we generalize this combinatorial approach to metamaterials with more than one zero-energy mode. To this end, we introduce a unit cell (Fig. 2*A*) with two zero-energy modes (Fig. 2 *B* and *C*). A central ingredient in combinatorial design is that the unit cells have fewer symmetries than that of the lattice they live on. In the present case, the unit cell does not have any planar rotational symmetry. Thereby, it can be tiled in four different orientations on a square lattice (Fig. 2*D*), in turn, allowing us to construct a wide range of combinatorial metamaterials.

We first analyze the combinatorial landscape of the metamaterials and notice that the design space is extremely large;

Significance

Mechanical metamaterials are man-made materials with extraordinary properties that come from their geometrical structure rather than their chemical composition. For instance, they can be engineered to be extremely light and stiff; to shrink sideways when compressed, instead of expanding; or to exhibit programmable shape changes. Such properties often rely on zero-energy modes. In this work, we created a class of mechanical metamaterials with zero-energy modes that can exhibit multiple properties at the same time within a single structure. In particular, we created a metamaterial that can either shrink or expand on the side when compressed, depending on how fast it is compressed. These metamaterials could lead to novel adaptable devices for, for example, robotics and energy absorption applications.

Author contributions: A.B., D.M.J.D., and C.C. designed research; A.B., D.M.J.D., J.v.d.L., and C.C. performed research; A.B., D.M.J.D., and C.C. analyzed data; and A.B., D.M.J.D., and C.C. wrote the paper.

The authors declare no competing interest.

This article is a PNAS Direct Submission. K.B. is a guest editor invited by the Editorial Board.

[1]A.B. and D.M.J.D. contributed equally to this work.

[2]To whom correspondence may be addressed. Email: coulais@uva.nl.

This article contains supporting information online at https://www.pnas.org/lookup/suppl/doi:10.1073/pnas.2018610118/-/DCSupplemental.

Published May 17, 2021.

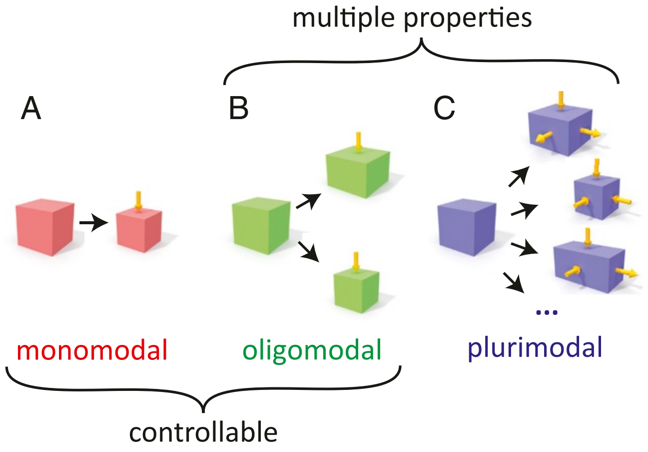

Fig. 1. Oligomodal materials. (*A*) Monomodal materials have a single zero-energy mode, hence a single property, that can be obtained via a simple actuation protocol. (*B*) Oligomodal materials have a small but fixed number of zero-energy modes larger than one, hence a few distinct properties, that can be selected with a simple actuation protocol, for example, uniaxial compression. (*C*) Plurimodal materials have a large number of zero-energy modes that grows with system size, and hence are kinematically able to host a large number of properties, but they often require complex actuation protocols, for example, multiaxial loading.

that is, for an $n \times n$ tiling, there are 4^{n^2} possible configurations. It is thus impossible to sample all of the possible configurations, even numerically. Therefore, we restrict our attention to a subset of configurations. Namely, we will focus on periodic tilings of 2×2 supercells (Fig. 2*E*), which is a very small fraction of the design space; we discuss an example of quasiperiodic tilings in *SI Appendix*. Any choice of four orientations defines a 2×2 supercell and thus a tiling; hence there are 256 possible configurations. By using the isometries of the square, we can reduce these to only 10 mechanically nonequivalent configurations (Fig. 2*F*). A numerical study of the kinematics (*Materials and Methods*) then reveals a rich spectrum of zero-energy modes. This spectrum contains the three classes of metamaterials defined in Fig. 1. For system sizes $n > 4$, monomodal tilings (Fig. 2 *G* and *H*, red) have a single zero-energy mode; oligomodal tilings have a constant zero-energy mode number larger than one (Fig. 2 *G* and *I*, green); and plurimodal tilings have a number of zero-energy modes that increases linearly with n (Fig. 2 *G* and *J*, blue).

All three classes of tilings share a common zero-energy mode, which is the rotating-squares mechanism (13), which spans the size of the system, and where the unit cells have the same deformation in an alternating manner with a lattice spacing periodicity of two (Fig. 2*H*). Monomodal tilings only have this zero-energy mode, while oligomodal and plurimodal tilings have additional zero-energy modes. In particular, plurimodal tilings include most periodic tilings and feature modes that are typically localized along lines (Fig. 2*J* and *SI Appendix*), which we term *line modes*. The existence of line modes in a periodic tiling implies that such a tiling is plurimodal, and explains why the number of modes grows with the size of the sample n. Such lines modes have, in fact, previously been identified in highly symmetric lattices (14, 15), and highly localized deformations related to line modes have been observed in foams under compression (16–22). We discuss a particularly intriguing example of nonperiodic plurimodal tilings, in *SI Appendix*, namely, a quasi-crystalline tiling that gains a single zero-energy line mode when its side length is doubled, thus leading to a number of modes that scales logarithmically with the size of the sample n.

Oligomodal Tilings

In contrast to the highly localized line modes, the additional zero-energy modes present in oligomodal tilings are markedly different: They typically exhibit deformations covering the whole sample (Fig. 2*I*). By definition, their number remains constant with increasing system size. There is, in principle, no upper bound on the number of modes in an oligomodal tiling, but, by construction, this number of modes in the tiling cannot exceed the number of modes in the supercell. These spatially extended deformations, which, to the best of our knowledge, have not been reported before, offer the prospect of unconventional bulk properties.

In the following, we focus on the simplest oligomodal configuration that we uncovered: the bimodal tiling of Fig. 3*J*, which hosts two bulk zero-energy modes irrespective of system size. In order to understand the nature of these zero-energy modes (and, in fact, also to interpret and classify all three classes of tilings; see *SI Appendix*), we introduce a vertex representation that maps out

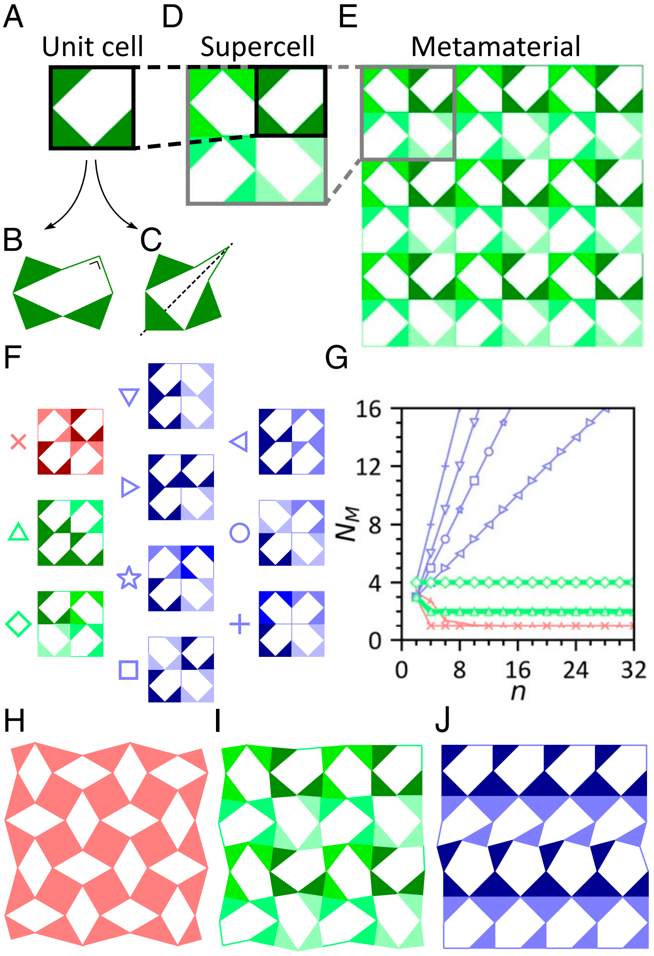

Fig. 2. Combinatorial design space. (*A*) Bimodal unit cell that has two zero-energy deformation modes. (*B*) Mode 1, actuating four angles, with constant square angle indicated. (*C*) Mode 2, actuating all five angles, with dashed symmetry line. (*D*) The 2×2 supercell made up from stacking the unit cell in four possible orientations. (*E*) Periodic 6×6 metamaterial made from stacking a 2×2 supercell. (*F*) All mechanically nonequivalent 2×2 supercells, featuring monomodal (red), oligomodal (green), and plurimodal (blue) mode scalings. (*G*) Mode scaling, N_M, with the tiling's side length, n, for all 10 tilings in *D* and the average of random tilings (red triangular crosses). (*H*) Rotating-squares mechanism of monomodal tilings. (*I*) Spatially extended mode typical of oligomodal tilings. (*J*) Line localized mode typical of plurimodal tilings.

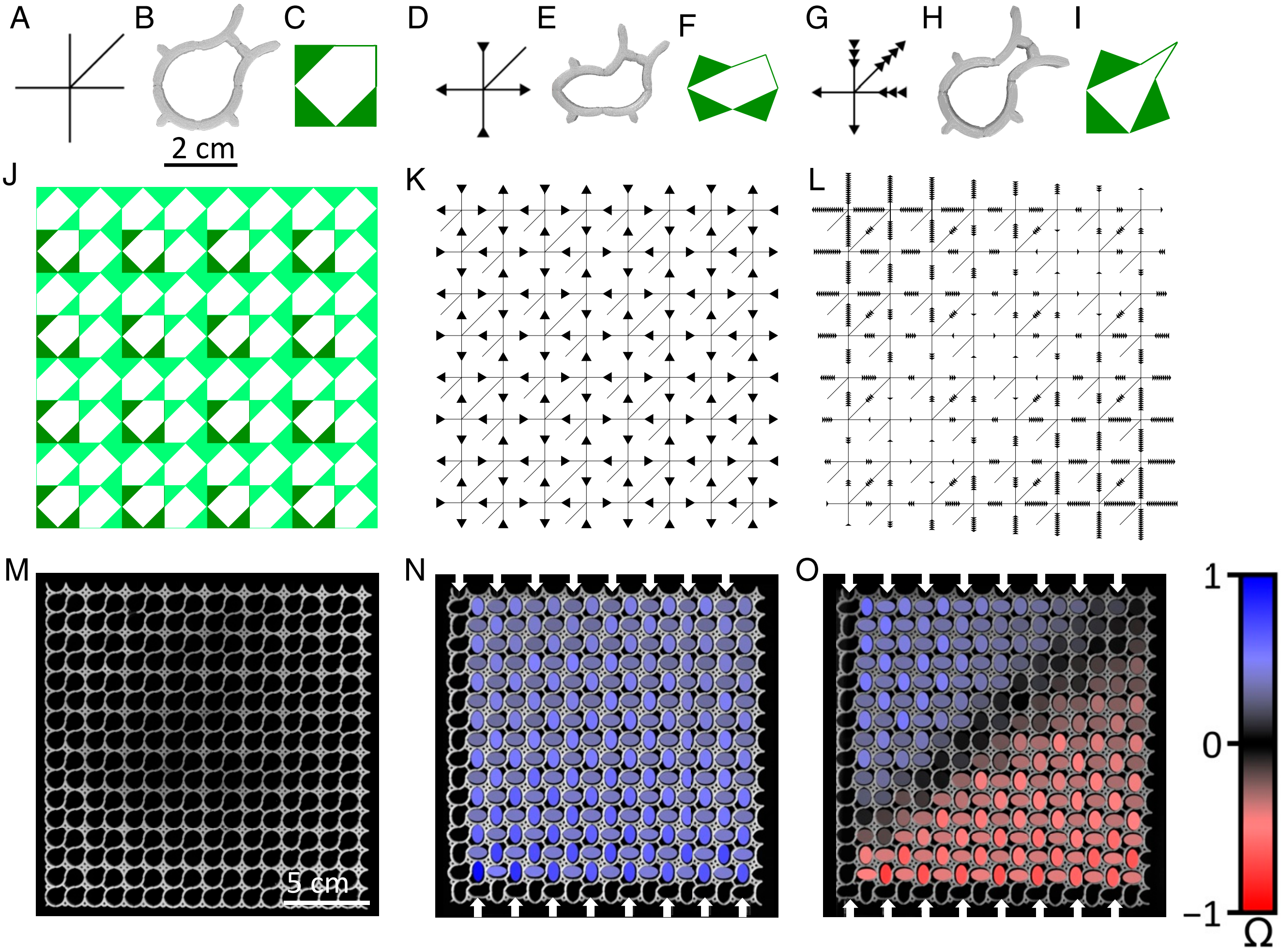

Fig. 3. Oligomodal metamaterials. (*A*–*I*) Unit cell of Fig. 2*A* in vertex (*A*, *D*, and *G*), 3D-printed (*B*, *E*, and *H*), and schematic representation (*C*, *F*, and *I*) in undeformed (*A*–*C*), deformed in its first mode (*D*–*F*), and deformed in its second mode (*G*–*I*) configurations. (*J*–*L*) The 8 × 8 schematic oligomodal metamaterial design (*J*), with rotating-squares mode (*K*) and bidomain mode (*L*) visualized in vertex representation. (*M*–*O*) The 16 × 16 oligomodal metamaterial sample at rest (*M*), and subjected to textured boundary conditions 1 (*N*) and 2 (*O*) (white arrows). Colored ellipses indicate hole polarization Ω defined in *Selective Actuation by Textured Boundaries*. See also Movie S1.

angle deformations onto a directed graph, that is reminiscent of vertex models found in two-dimensional (2D) statistical physics (23–25) (*Materials and Methods*). This representation allows for a simple graphical representation of single-cell deformations. Each vertex corresponds to a unit cell, each edge corresponds to a hinge, and the number of arrowheads on each edge quantifies the hinge deformation (Fig. 3 *A*, *D*, and *G*). In this representation, the geometric constraints can be formulated as follows: Only linear combinations of the two vertices shown in Fig. 3 *D* and *G* are allowed. These geometric constraints are propagated from one vertex to its neighbors via the edges, through a combinatorial search. Unlike the standard structural analysis computation that we used to predict the number of zero-energy modes shown in Fig. 2*G* (*Materials and Methods*), the vertex model provides direct insight into the spatial shape of the possible soft deformation modes. Performing such an analysis on the oligomodal tiling shown in Fig. 3*J* reveals two distinct system-spanning zero-energy modes. First, we find the rotating-squares mode (Fig. 3*K*) as expected, using the first unit cell mode of Fig. 3 *D*–*F* only. Second, we find a new bulk bidomain zero-energy mode, which features a symmetry axis going from southwest to northeast, splitting the deformation into two domains (Fig. 3*L*), combining both unit cell modes of Fig. 3 *D*–*I*. This mode spans the size of the system, with a constant gradient of deformation along the southeast to northwest axis. Therefore, for a tiling that would be twice as large, the gradient of deformation would the same, and the deformation would be twice as large. If the tiling were rectangular, the gradient of deformation would remain the same, oriented in the southeast to northwest axis. In the remainder of the paper, we use the oligomodal geometry with two distinct zero-energy modes to create flexible metamaterials with two distinct soft deformation modes. We demonstrate that we can selectively actuate these soft deformation modes—and thus obtain two distinct effective mechanical properties—by using either boundary texture or strain rate-dependent viscoelasticity.

Selective Actuation by Textured Boundaries

First, we demonstrate that sets of suitably chosen textured boundary conditions under simple uniaxial compression allow preferential exciting of a zero-energy mode of choice while frustrating the others. Using multimaterial 3D printing, we create a metamaterial made of 16 × 16 unit cells (Fig. 3*M*), following the oligomodal tiling of Fig. 3*J*. The 3D-printed unit cells are made of rigid curved struts and compliant hinges (Fig. 3*B*; see *Materials and Methods* for details), such that their shapes coincide with the idealized unit cell (Fig. 3*C*). Crucially, the 3D-printed unit cells have two soft deformation modes (Fig. 3 *E* and *H*) that closely mimic the zero-energy modes of the idealized unit cell (Fig. 3 *F* and *I*). Following the deformation prescribed by the vertex representation (Fig. 3 *K* and *L*), we then compress our metamaterial using two sets of eight indenters on each side, that apply the load on every other unit cell and where the bottom set of indenters is either antialigned (Fig. 3*N*) or aligned (Fig. 3*O*) with the top set of indenters. To quantify the deformations of each unit cell, we use particle tracking (OPENCV [a computer vision library] and Python) and custom-made tracking algorithms to quantify the flattening f and orientation ϕ with respect to the horizontal of each pore and calculate the polarization (26) $\Omega := (-1)^{n_x+n_y} f \cos 2\phi$, where n_x (n_y) is the unit cell's column (row). Using this protocol, we observe that we can actuate either the rotating-squares mode (Fig. 3*N*) or the bidomain mode (Fig. 3*O*) by changing the location of load application (see also Movie S1). This example demonstrates that the zero-energy modes of oligomodal metamaterials can be selectively actuated by tuning the boundary texture. In the following, we build on this result to achieve mode selection under a simpler actuation protocol that does not resort to boundary texture.

Selective Actuation by Dissipation

To achieve this goal, we leave the realm of static responses and harness viscoelastic dissipation to tune the dynamical response of our metamaterial (26–28), previously applied to alter the direction of a mechanical mode (26, 28). Instead, we now harness viscoelasticity to switch between modes altogether. To this end, we use the oligomodal metamaterial design of Fig. 3*J*, which we rotate by 45° (Fig. 4 *A*–*D*). With this rotation of the lattice, we expect the domain wall seen in Fig. 3*O* to rotate by 45° (Fig. 4 *B* and *D*), and thus to become perpendicular to the loading axis as well as to provide mirror symmetry about the transverse axis.

The selective actuation of modes via viscoelasticity is possible because the two modes—the rotating-square mechanism (Fig. 4 *A* and *C*) and the bidomain mode (Fig. 4 *B* and *D*)—involve distinct sets of hinges. While, in the rotating-square mechanism, all hinges but the one at the center of the supercell are actuated (white hinges in Fig 4*A*), in the bidomain mode, all hinges including the one at the center of the supercell are actuated (white and black hinges in Fig 4*B*). Therefore, in order to favor the actuation of the rotating-squares mechanism (respectively, the bidomain mode), the central hinge should be stiffer (respectively, softer) than the other hinges. Conversely, in order to favor the actuation of the bidomain mode, the central hinge should be softer than the other hinges. To obtain a selective actuation of the modes, we tune the stiffness of hinges by making them viscoelastic. Specifically, we use 1) viscoelastic hinges—whose stiffness increases with the strain rate at which they are actuated—for the hinges that are actuated in the rotating-squares mechanism (white hinges in Fig 4 *A* and *B*) and 2) elastic hinges—whose stiffness does not depend on the strain rate at which they are actuated—for the hinge that is only actuated in the bidomain mode (black hinge in Fig 4*B*).

Next, we prove the feasibility of the concept described above with finite element simulations (Abaqus; see *Materials and Methods* and *SI Appendix*). In order to selectively actuate one mode or the other, we use a combination of stiff material for the rigid parts and soft material for the compliant hinges. In particular, we dress our metamaterial with two types of elastic and viscoelastic hinges (see Fig. 9*B*) whose properties correspond to (visco)elastic elastomers we will use in the experiments (Fig. 5 *A* and *B*; see *Materials and Methods* for details about the simulations). For slow actuation rates, both types of compliant hinges have a very similar torsional stiffness (*Materials and Methods*). When the actuation rate increases, the viscoelastic hinges stiffen dramatically: They become more than 5 times stiffer than the elastic hinges (*Materials and Methods*). As expected, we find that,

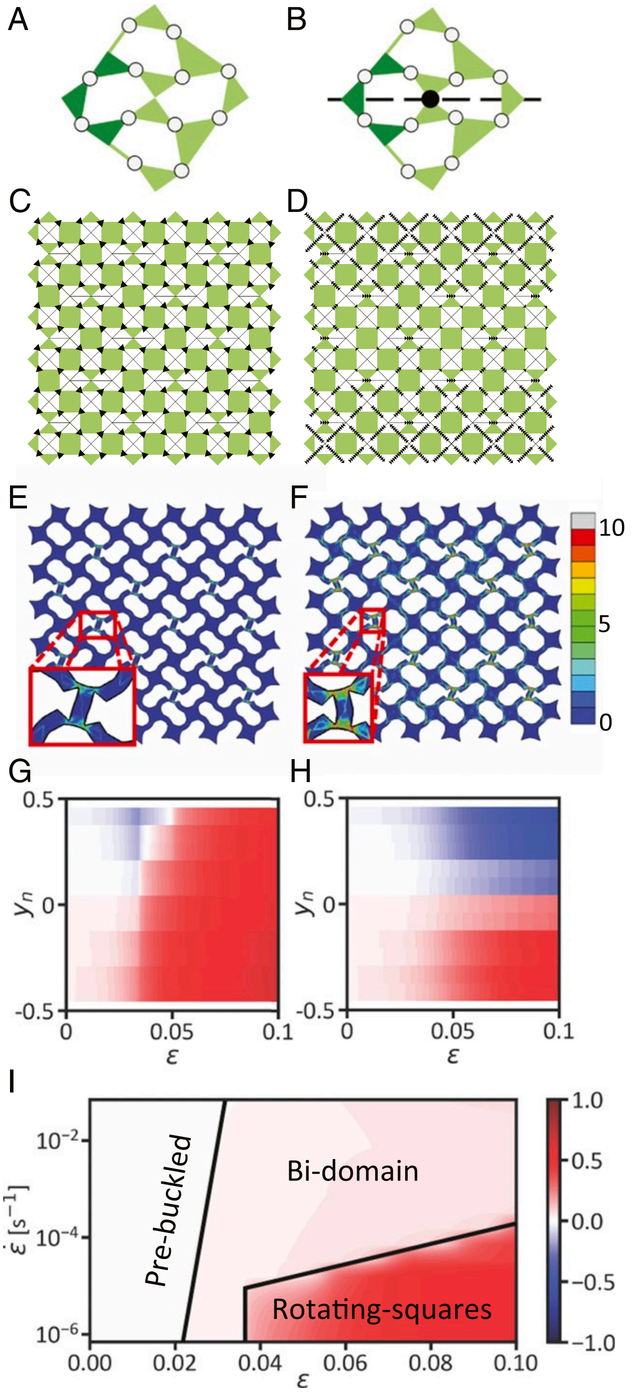

Fig. 4. Mode selection using strain rate. (*A*–*D*) Schematic supercell representation (*A* and *B*) and schematic and vertex model representation (*C* and *D*) of the rotating-squares mode expected under slow actuation (*A* and *C*) and of the bidomain mode expected under fast actuation (*B* and *D*). The tiling design follows Fig. 3, but is rotated by 45°. (*E* and *F*) Numerical realization of the schematic sample of *C* and *D*, numerically compressed in vertical direction to 7% strain with an average strain rate $\dot{\varepsilon} = 9.3 \cdot 10^{-6}\,\mathrm{s}^{-1}$ (*E*) and $\dot{\varepsilon} = 0.11\,\mathrm{s}^{-1}$ (*F*). The legend indicates the Von Mises stress (megapascals). *Insets* contain enlarged views of an individual hinge. (*G* and *H*) For the cases of *E* and *F*, respectively, the average hole row polarization Ω as function of strain ε, up to 10% strain, and normalized vertical coordinate y_n. The polarization is defined as $\Omega := (-1)^{n_y} f \cos 2\phi$, where n_y is the unit cell's row, starting at zero at the bottom; f is the flattening of the ellipse; and ϕ is the orientation of the ellipse with respect to the first diagonal. (*I*) Absolute value of the average sample polarization Ω as function of strain ε and strain rate $\dot{\varepsilon}$. The legend indicates the average row hole polarization Ω for *G*–*I*.

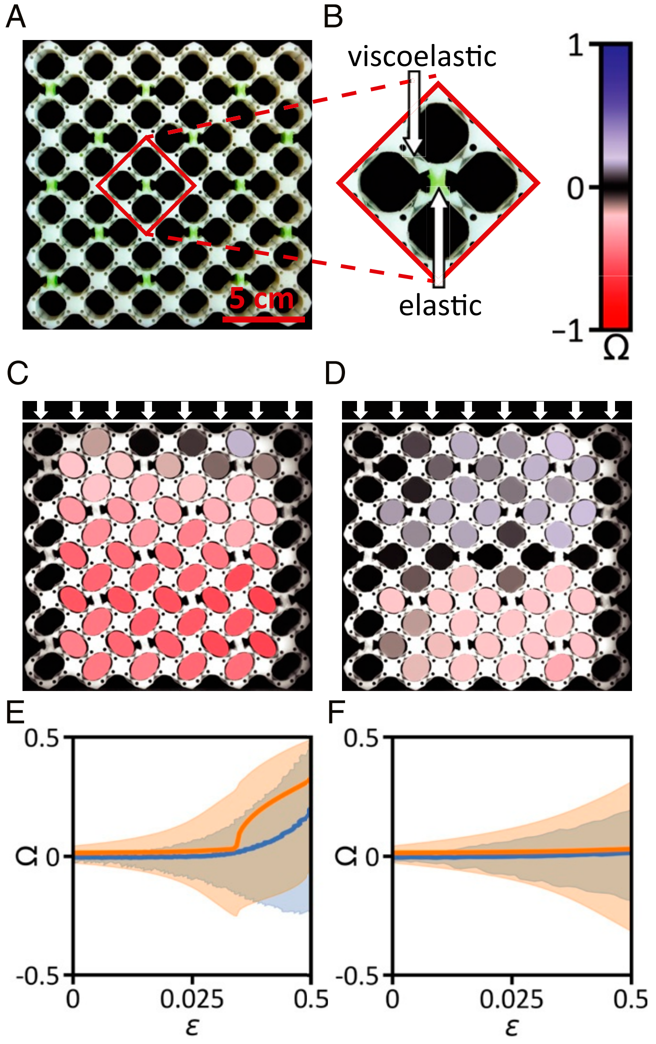

Fig. 5. Experimental validation of mode selection mediated by strain rate. (*A*) Oligomodal metamaterial made of rigid (white), elastic (green) and viscoelastic (transparent) material at rest, following the sample design of Fig. 4 *E* and *F*. (*B*) Close-up of *A*, on a 2×2 supercell. (*C*–*F*) Response of oligomodal metamaterial under slow (*C* and *E*) and fast (*D* and *F*) compression rates. (*C* and *D*) Snapshot of the metamaterial and overlaid reconstructed pores after a compression $\varepsilon = 0.056$ at a strain rate $\dot{\varepsilon} = 9.3 \cdot 10^{-6}\mathrm{s}^{-1}$ (*C*) and $\dot{\varepsilon} = 0.11\ \mathrm{s}^{-1}$ (*D*). The colors of the ellipses indicate the polarization, in line with the legend, as defined in Fig. 4. While $\Omega = 0$ (black) corresponds to no polarization and hence no deformation, $\Omega = \pm 1$ (red and blue) correspond to highly polarized and deformed pores. See also Movie S2. (*E* and *F*) Corresponding average sample polarization Ω with maximum and minimum spread as function of strain ε: experimental results in blue, and numerical results, following the results of Fig. 4, in orange.

on the one hand, compressing the metamaterial at a low strain rate with respect to the relaxation timescales of the viscoelastic material of $\dot{\varepsilon} = 9.3 \cdot 10^{-6}\,\mathrm{s}^{-1}$ leads to deformations that follow the rotating-squares mechanism (Fig. 4 *E* and *G*). On the other hand, compressing the metamaterial at a large strain rate with respect to the relaxation timescales of the viscoelastic material of $\dot{\varepsilon} = 0.11\,\mathrm{s}^{-1}$ leads to deformations that follow the bidomain mode (Fig. 4 *F* and *H*). A closer look at the central hinge of the supercell (Fig. 4 *E* and *F*, *Insets*) reveals that this hinge is not actuated for low strain rates (Fig. 4 *E*, *Inset*) and actuated for large strain rates (Fig. 4 *F*, *Inset*), which is consistent with the mechanism of mode selection described above.

Moreover, we confirm that the mode selection is applicable across a wide range of strains, including at large strains (10% strain). Both small and large strain rates initially buckle at a strain of $\varepsilon \approx 0.02$ into the bidomain deformation (Fig. 4 *G*–*I*), as can be seen from the presence of two domains of opposite polarization Ω in the top and bottom of the sample (blue and red regions in Fig. 4 *G* and *H*), which then builds up an average polarization that remains close to zero (light red region in Fig. 4*I*). This first deformation mode is due to the fact that the sample has been designed with a small imperfection aimed at favoring the bidomain mode (see *SI Appendix*). At low strain rates, however, the sample ultimately deforms into the rotating-squares mode, as can be seen from the uniform distribution of polarization (red region in Fig 4*G*), which then builds up a large average polarization (red region in Fig 4*I*). A systematic scan of various strain rates (Fig 4*I*) reveals the following: 1) We find a sharp transition between the actuation of the rotating-squares mode (at low strain rates) and the actuation of the bidomain mode (at large strain rates). While the fact that strain rate allows selection of the mode was expected from our arguments above, the fact that the transition is sharp is more surprising. At this transition, the deformations abruptly snap from the bidomain mode toward the rotating-squares mode, as can be seen from the drastic change of polarization. 2) We find that the onset of buckling toward the rotating-squares mode is shifted to larger values of strains at larger strain rates.

This shift is the result of a relatively lower stiffness of the bidomain actuated elastic hinges with respect to the viscoelastic hinges. Hence, the imperfection favoring the bidomain mode is more difficult to overcome at higher strain rates, and buckling occurs at larger strains.

We use the numerical results described above for the design of our experiments, and we fabricate a metamaterial with plastic rigid parts, viscoelastic hinges, and elastic hinges (Fig. 5 *A* and *B*) using a combination of 3D-printing, molding, and casting techniques (see *Materials and Methods*). We compress the metamaterial slowly at a strain rate of $\dot{\varepsilon} = 9.3 \cdot 10^{-6}\mathrm{s}^{-1}$ and indeed observe that the metamaterial responds in the rotating-squares mode (Fig. 5*C*). The polarization Ω, overlaid on the experimental pictures, allows clear visualization of the overall negative polarization corresponding to the rotating-squares mode (see also Movie S2). We also compress the metamaterial fast at a strain rate of $\dot{\varepsilon} = 0.11\ \mathrm{s}^{-1}$ and now observe that the metamaterial responds in the bidomain mode (Fig. 5*D*). Indeed, the overlaid polarization clearly splits into two domains separated by a relatively undeformed region. Tracking the polarization in Fig. 5 *E* and *F* for small and large strain rates, respectively, shows that the simulations and experiments are in qualitative agreement. First, the applied bidomain mode imperfection (see *Materials and Methods* and *SI Appendix*) always induces a bidomain mode deformation, with a widening polarization range, centered around $\Omega = 0$. Then, small strain rates excite increasing average polarizations postbuckling toward the rotating squares mode above $\varepsilon > 0.03$ in Fig. 5*E*, while the symmetry of the bidomain mode keeps the average polarization close to zero at all strain values in Fig. 5*F*. However, in both cases, it appears that buckling occurs earlier numerically than experimentally. This could be because the numerical model neglects the hinge bonds' flexibility and is therefore more prone to buckling, or the experimental imperfections favor the bidomain deformation less.

In conclusion, the combination of oligomodal architectures and viscoelastic hinges provides a robust strategy to achieve mode selection by strain rate, which can be designed with the help of finite element methods. Employing an oligomodal tiling is crucial to achieve such controlled mode selection; indeed, the many additional localized modes present in plurimodal tilings could introduce unwanted degrees of freedom that perturb the mechanical response.

Strain Rate-Dependent Poisson's Ratio

In this last section, we ask whether the selection of distinct modes can also lead to selection of distinct mechanical properties. Specifically, we probe whether the rotating-squares mechanism and the bidomain modes lead to distinct values of the Poisson's ratio, and, therefore, whether one can obtain distinct values of the Poisson's ratio using strain rate. Intuitively, we expect the presence of the domain wall to frustrate the overall lateral deformation and therefore to induce a larger Poisson's ratio for the bidomain mode than for the rotating-squares mechanism—see *Materials and Methods*.

We measure, both experimentally and numerically, the Poisson's ratio as a function of the strain ε for the same different strain rates as before. While we always find a positive Poisson's ratio in the prebuckling phase, we find that compressing at a small strain rate leads to a response with a negative nonlinear Poisson's ratio at strains $\varepsilon > 0.04$ (Fig. 6*A*, blue), while compressing at large strain rate induces larger values of the Poisson's ratio (Fig. 6*B*, blue). To obtain more insight on these results, we measure the Poisson's ratio as a function of the strain ε and the strain rate $\dot{\varepsilon}$ from the numerical simulations (Fig. 6 *A* and *B*, orange and Fig. 6*C*) and find that the Poisson's ratio remains positive in the prebuckled region, while it becomes negative in the buckled region. The rotating-squares mechanism and the bidomain mode both exhibit negative Poisson's ratios, yet the Poisson's ratio is larger and therefore less negative in the case of the bidomain mode, which is consistent with the experiments. Notably, the Poisson's ratio in the rotating-square mode shows larger spatial dispersion; this is a signature of the snapping transition that occurs when the deformation snaps from the bidomain mode into the rotating-square mode. Interestingly, as the buckling strain is pushed to larger values for larger strain rates, there is a range of strains $\varepsilon \in [0.3, 0.45]$ for which the Poisson's ratio can switch from positive to negative by tuning the strain rate. Therefore, there is a range of strains for which our metamaterial is multifunctional, hosting several functions that can be selected with a robust actuation protocol: auxetic under slow compression rate and nonauxetic at fast compression rate.

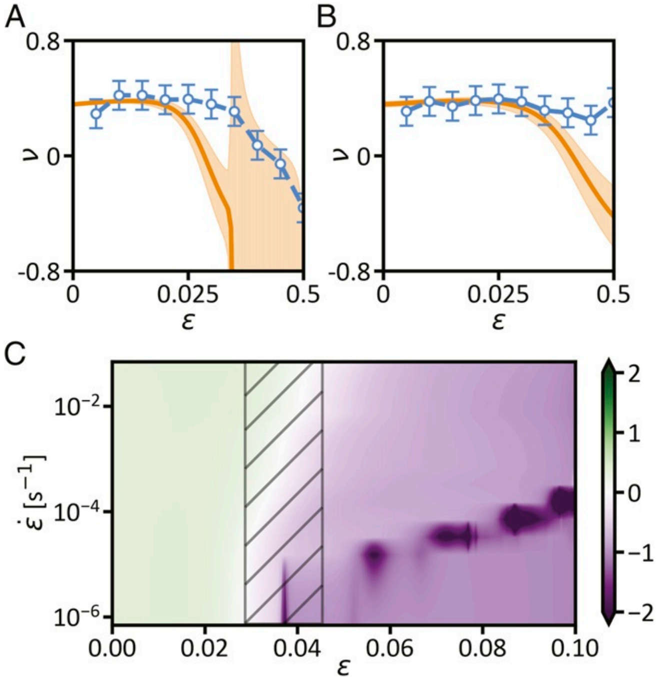

Fig. 6. Strain rate-dependent Poisson's ratio. (*A* and *B*) The average Poisson's ratio ν, as function of ε for the experimental sample of Fig. 5 *C* and *D* (blue, with error bars) and numerical sample Fig. 4 *E* and *F* (orange, with spatial spread) at a strain rate of $\dot{\varepsilon} = 9.3 \cdot 10^{-6}\ \mathrm{s}^{-1}$ (*A*) and of $\dot{\varepsilon} = 0.11\ \mathrm{s}^{-1}$ (*B*). (*C*) The absolute value of the average sample Poisson's ratio ν as function of strain ε and strain rate $\dot{\varepsilon}$ for the numerical sample of Fig. 4 *E* and *F*. The hashed area indicates the range of ε and $\dot{\varepsilon}$, where positive–negative Poisson's ratio switching can be observed.

Discussion

To conclude, we have introduced a class of materials, oligomodal metamaterials, that strike a delicate kinematic balance that allows them to exhibit a limited number of zero-energy modes. Based on these zero modes, we have created flexible metamaterials, whose deformations can then be selectively and robustly actuated using relatively simple loading protocols such as uniaxial compression, thus providing an example of multifunctional mechanics.

Our approach is fundamentally different from and is complementary to recent developments based on poroelasticity (29) and magnetoelasticity (30). In these works, multifunctionality is achieved through elaborate actuation multiphysics couplings and via loading in the bulk: The loading is exerted on the bulk by external fields, such as a chemical potential or a magnetic field. This is different from our case, where the deformation modes are selected in a purely mechanical fashion, and where the loading is exerted at the boundaries. These approaches could, in fact, benefit from employing oligomodal architectures, in order to reduce the number of involved degrees of freedom to the minimum required by the desired functions.

Our approach is broadly applicable for the design of flexible metamaterials with low-energy strain pathways. In particular, our approach could be further generalized to other types of unit cells, to other lattices, and to 3D tilings and applied to more types of functionalities such as chiral responses (31–33), shape morphing (4, 11, 34), enhanced energy absorption (26, 35) and nonlinear wave propagation (36, 37). In particular, we expect the switchable nature of oligomodal metamaterials to enable the control of deformation pathways, which could be potentially useful for dissipation of energy. Moreover, there is no reason to assume that a zero-energy mode-based method as we use is the only way to design flexible oligomodal metamaterials. Alternative analysis and design methods that can induce clear modal separation, such as topology optimization, may be used instead. Also, our design space, mostly restricted to periodic tilings of 2×2 supercells, could be dramatically augmented, for instance, by considering periodic tilings of larger supercells, by using alternative nonperiodic tiling strategies constructed via fractal substitution rules and mirroring (see *SI Appendix* for an example), or by harnessing defects (12, 38). Finally, data-driven approaches such as machine learning could provide a powerful alternative to better understand the structure–property relationship (33) and to rationally design oligomodal tilings. Additional open questions that remain are how to effectively design large deformation responses, which variety of multifunctionality can be achieved, and how to produce these materials on a large scale effectively.

Materials and Methods

Kinematics of Multimode Combinatorial Metamaterials. Repeating our bimode cell with arbitrary orientations on a square lattice yields a large variety of configurations. To understand how the balance between constraints and degrees of freedom gives rise to zero-energy modes and states of self-stress, we use the Maxwell–Calladine index theorem (14). It provides a relation between the number of states of self-stress N_{SS}, the number of zero-energy modes N_M, the dimension d, the number of hinges N, and the number of constraints c,

$$dN - c = \frac{d(d+1)}{2} + N_M - N_{SS}, \qquad [1]$$

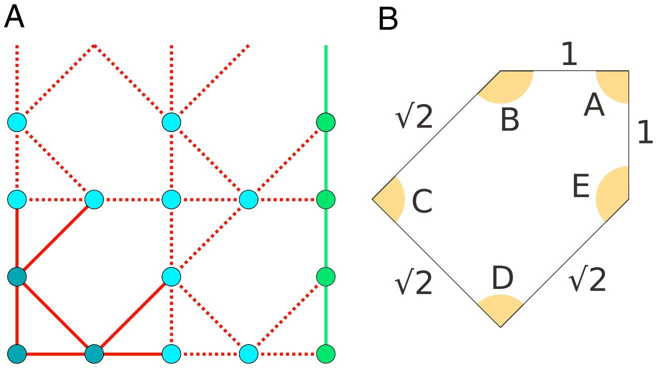

Fig. 7. Kinematics of the unit cell. (*A*) Counting the constraints and degrees of freedom. Each cell contributes $N=3$ points (dark blue points) and $c=7$ constraints (solid red lines). Light blue points and dashed lines represent contributions from other cells. Boundary cells additionally contribute $N=2$ points and $c=2$ constraints, in green. (*B*) Geometry and parametrization of the five-bars linkage, which constitutes the functional backbone of the bimodal unit cell.

which we can evaluate for arbitrary choices of cell orientations. In a tiling of $n\times n$ cells, each cell has a contribution of $N=3$ and $c=7$, with an additional contribution of $N=4n+1$ and $c=4n$ from the boundary (Fig. 7*A*). Constraining displacements to the plane, this yields

$$N_M-N_{SS}=4n-n^2-1. \qquad [2]$$

Since the number of zero-energy modes N_M cannot be negative, Eq. **2** implies a lower bound for the number of states of self-stress of n^2-4n+1. Thus, to leading order, the number of states of self-stress is extensive. Eq. **2** provides a negative lower bound for N_M, which hence is poor. In order to obtain more information on the number of zero-energy modes, one has to go beyond the Maxwell–Calladine index theorem by computing the kernel of the compatibility matrix explicitly (14). Applying the compatibility matrix on a vector containing the displacements of the hinges produces a vector that describes the corresponding stretching of the bars. Therefore, any displacement vector in the kernel of this matrix produces no stretching whatsoever, making it a zero-energy mode. To obtain the mode scalings displayed in Fig. 2*G*, we calculated the nullity of the compatibility matrix numerically using the LAPACK (Linear Algebra PACKage) driver xGESDD (a divide-and-conquer singular-value decomposition method).

Vertex Model. The approach described above has, however, a drawback: It yields arbitrary superpositions of the zero-energy modes, potentially providing very little insight on the nature of the involved deformations. To complement this standard method, we therefore introduced an approach in *Oligomodal Tilings*, based on graphs with directed edges. We now derive this approach in detail, starting from the fully nonlinear geometric constraints of the primitive cell. They can be encoded in three trigonometric equations, namely,

$$A+B+C+D+E=3\pi, \qquad [3]$$

$$1-\cos(A)=3-2\cos(C)-2\cos(D)+2\cos(C+D), \qquad [4]$$

$$\sin(D)-\frac{\sin(D+E)}{\sqrt{2}}=\sin(C)-\frac{\sin(C+B)}{\sqrt{2}}, \qquad [5]$$

where the angles A, B, C, D, and E are defined in Fig. 7*B*. To construct the directed graph model, we perform a few algebraic manipulations and linearization. First, we change variables and consider

$$A=\frac{\pi}{2}+\alpha \quad B=\frac{3\pi}{4}+\beta$$
$$C=\frac{\pi}{2}+\gamma \quad D=\frac{\pi}{2}+\delta \quad E=\frac{3\pi}{4}+\varepsilon. \qquad [6]$$

Then, we linearize Eqs. **4** and **5** in α, β, γ, δ, and ε. This linearization around the rest position of our primitive cell yields

$$\begin{pmatrix}\alpha\\ \delta\\ \varepsilon\end{pmatrix}=\begin{pmatrix}-2&-2\\ -1&-2\\ 2&3\end{pmatrix}\begin{pmatrix}\beta\\ \gamma\end{pmatrix}. \qquad [7]$$

As expected from the index theorem, there are two free parameters. We then pick a convenient basis

$$\begin{pmatrix}\beta\\ \gamma\end{pmatrix}=\chi\begin{pmatrix}-1\\ 1\end{pmatrix}+\xi\begin{pmatrix}3\\ -1\end{pmatrix}. \qquad [8]$$

This equation allows designing of Fig. 3 *A*, *D*, and *G*. We draw the cell as a vertex with five edges, one for each hinge, and make use of the fact that only integer coefficients appear in Eq. **7** to draw arrows on the edges. Setting $\xi=0$ ($\chi=0$), we draw n arrows on an edge if the corresponding angle is equal to $n\chi$ ($n\xi$). We draw the arrows as incoming for positive angles and outgoing for negative angles. This produces the directed vertex of Fig. 3*D* (Fig. 3*G*). Any linear combination of those two configurations also produces a compatible vertex. The final ingredient in our model consists in remarking that every hinge is also subject to angle conservation, allowing us to concatenate single-cell graphs to obtain a directed graph describing the full tiling (Fig. 3 *K* and *L*).

Importantly, by an angle-fixing argument, the model could be trivially extended to six, seven, and eight edges per vertex by taking our existing vertex and adding a diagonal edge in either of the three available corners. If we then fix the value of one of these diagonal edges, we reduce the problem to the pentagonal case. Since this yields three, four, or five independent vertices, it exhausts the number of available zero-energy modes. In principle, this linearization procedure is also applicable to other primitive cells, and provides a convenient graphical tool in the cases for which the resulting coefficients are integers.

Finite Mechanisms and Infinitesimal Zero-Energy Modes. We discuss here the nature of the zero-energy modes determined above. Two classes of zero-energy modes can exist (14): 1) the finite mechanisms, in which the zero-energy deformations can persist in the nonlinear regime and lead to large rotations without stretching or compressing any bars; 2) infinitesimal zero-energy modes, in which the deformations are only zero-energy in the linear range. Further deformations in the nonlinear regime typically cost elastic energy through elongation of the rods. As demonstrated in our experiments, such infinitesimal modes translate to soft deformation modes in practice.

A visual inspection of the kinematics of the elementary modes in *SI Appendix*, Table S1 reveals that only the rotating-squares mode is finite. All of the other zero-energy modes require length change of the rods to be extended into the nonlinear regime and, as such, are infinitesimal.

Sample Design and Fabrication. The 16×16 samples of Fig. 3 *M*–*O* are designed following the tilings shown in Fig. 3*J*. The samples' dimensions are $192\times192\times4$ mm. The 6×6 sample of Fig. 5 is designed following the same tiling shown in Fig. 3*J*, rotated by 45°. The sample's dimensions are $180\times180\times20$ mm.

For these two types of samples, special care has been devoted to the design of the details of the unit cells: Imperfect compliant hinges, experiencing shear and tension instead of pure bending/torsion, can affect

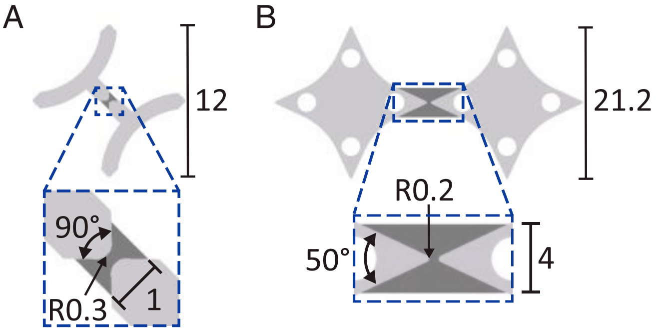

Fig. 8. Compliant hinge geometry. (*A*) Hinge geometry of Fig. 3. (*B*) Hinge geometry of Fig. 5. The light gray (dark gray) material is rigid (compliant). All units are in millimeters unless otherwise specified.

https://doi.org/10.1073/pnas.2018610118

Table 1. Mechanical properties of compliant hinges of Fig. 5

Stiffness		Elite double 32		Agilus 30	
		Fast	Slow	Fast	Slow
Bending	(Nmm/rad)	24	20	120	20
		±1	±2	±25	±2
Tension	(N/mm)	31	24	630	44
		±2	±1	±150	±10
Shear	(N/mm)	10	8.1	190	18
		±1	±0.4	±30	±3

Bending, tensile, and shear stiffness under fast (20 mm/s) and slow (0.002 mm/s) loading rate.

the linear and nonlinear deformation of mechanisms significantly (39). For the samples of Figs. 3 and 5, we negate these effects in two ways. First of all, the central unit cells are made from a much more rigid material than the elastic hinges, such that the central unit cells do not deform during loading. Next, we use tapered rigid parts as seen in Fig. 8. A central narrow section between the rigid sections greatly increases resistance to shear and tension while offering only a negligible resistance to bending.

When the actuation is aligned with the primitive lattice, the bidomain mode leads to shear–compression coupling. However, such a mode in a 45° orientation can lead to a positive Poisson's ratio, which is markedly different from the rotating-squares mode, that has a negative Poisson's ratio (*SI Appendix*). Therefore, we choose to rotate the sample by 45° in Fig. 5. Without imperfection, the configuration in Fig. 5 would have an inherent buckling preference toward the rotating-squares mode of Fig. 5*C*. However, this preference is tuned by designing an imperfection (40) favoring the bidomain mode of Fig. 5*D*, which has been designed using nonlinear viscoelastic finite element methods (Abaqus; see *SI Appendix*). Furthermore, as the samples are tested horizontally, the bottom of the sample features small pockets with 5-mm steel ball bearings to reduce the effects of friction with the bottom surface.

We produce the samples in Fig. 3 using additive manufacturing using a Stratasys Objet500 Connex3 3D printer. The hinges are produced from a highly viscoelastic rubber-like PolyJet Photopolymer (Stratasys Agilus 30), which is cocured with the central parts, which are made from a much stiffer Photopolymer (Stratasys VeroWhitePlus). The square hinges and central parts of the sample of Fig. 5 are produced in the same way. However, the triangular hinges of the sample of Fig. 5 are cast from an elastic two-component silicon-based rubber (Zhermack Elite Double 32), and are then glued to the sample using Wacker Elastosil E43 glue. We anticipate that advances in additive manufacturing, using, for instance, silicone resins, will allow single-step manufacturing of the elastic–viscoelastic samples of Fig. 5 in the near future.

Experimental Methods. We compress the periodic bimode sample in Fig. 3 *M–O* using a uniaxial testing device (Instron 5943 with a 500-N load cell), with laser-cut Plexiglas indenters, denoted by the white arrows in the figure, at a strain rate of $\dot{\varepsilon} = 1.30 \cdot 10^{-3} \mathrm{s}^{-1}$ to a strain of $\varepsilon = 0.026$. The sample is positioned horizontally to enhance overall mechanical stability, with gravity preventing out-of-plane buckling. The quasiperiodic sample in *SI Appendix*, Fig. S1 is produced and tested in a similar way. However, the sample is compressed, instead, in the direction from the upper left to the bottom right.

The sample in Fig. 5 is compressed using the same uniaxial testing machine with straight surfaces on the top and bottom, at various strain rates. The sample is also positioned horizontally to enhance overall mechanical stability, with gravity also preventing out-of-plane buckling. For Fig. 3 (Fig. 5), the tests are recorded using a high-resolution 3,858 × 2,748 (2,048 × 2,048) monochrome CMOS camera Basler acA3800-14um with Fujinon 75-mm lens (acA2040-90um with Fujinon 50-mm lens), inducing a spatial resolution of 0.07 mm (0.1 mm). Using particle tracking (OPENCV and Python), we extract and track the four central holes of the stiff sections, which we use to calculate the position and ellipticity of all of the pores, whose reconstruction has been overlaid in Fig. 3 (Fig. 5). For Fig. 5, we track the average horizontal (vertical) distance between the centers of the ellipses on the sides (top and bottom) to compute the width (height) of the sample, from which we extract the compressive axial strain $\varepsilon_{\mathrm{axial}}$ and the strain transverse to the loading direction, $\varepsilon_{\mathrm{transverse}}$. We use these quantities to compute the nonlinear Poisson's ratio $\nu := -\partial\varepsilon_{\mathrm{transverse}}/\partial\varepsilon_{\mathrm{axial}}$ averaged over applied strain deformation steps of $\delta\varepsilon_{\mathrm{axial}} = 0.005$.

Hinge Material Properties. We measure the mechanical properties of a single compliant hinge of the sample in Fig. 5 using the same uniaxial testing device. We perform three different experiments: bending, tension, and shear. For bending, we pull on the hinge up to 0.30-rad deflection at rates of 0.002 and 20 mm/s. For tension and shear, we pull on the hinge up to 1.0-mm deflection at rates of 0.002 and 20 mm/s. We report the average of the measured stiffnesses in Table 1.

We observe that the stiffnesses at long timescales are similar for both types of hinges. However, at short timescales, the stiffnesses of the elastic (Elite Double 32) hinges increases only by approximately 20 to 30% compared to long timescales, while the stiffnesses of the viscoelastic (Agilus 30) hinges can increase by more than 1,300%. This difference in loading-rate dependency allows us to obtain the switchable response observed in Fig. 5.

Simulating Oligomodal Metamaterials. We use dynamic explicit nonlinear finite element methods (Abaqus 2018, Dassault Systèmes) to predict and design the dynamic response of oligomodal metamaterials, as well as to study the effects of changing material and geometry parameters. We model the geometry of the sample of Figs. 4 and 5 as seen in Fig. 9 using 2D triangular quadratic elements (CPE6). Plane strain elements are used as the rigid material to prevent the hinges from expanding and contracting in reality (as in Fig. 5). A mesh density featuring at least four elements through the hinge thickness and at least eight elements through the hinge thickness at the center is used, after performing a mesh convergence study showing that mesh refinement leads to little to no differences in global deformation.

We model the stiff plastic components as a linear elastic material with a Young's modulus of $E = 1$ GPa and Poisson's ratio $\nu = 0.3$. The hinges are modeled as flexible nearly incompressible hyperelastic materials [Abaqus specific implementation of Arruda–Boyce material (41)], with a material large strain stiffening parameter $\lambda_m = 2$ and a Poisson's ratio $\nu = 0.47$, corresponding to a ratio of the bulk and shear modulus $K/\mu = 15.7$. The elastic hinges (black in Fig. 9*B*) have $E = 1$ MPa. The viscoelasticity of the viscoelastic hinges (gray in Fig. 9*B*) is accounted for using a three-term Prony series, with relaxation strengths $\eta_{123} = (0.45, 0.26, 0.10)$ and timescales $\tau_{123} = (0.047, 0.97, 18)\,\mathrm{s}^{-1}$ (26). To study the effects of changing material parameters, we vary the instantaneous Young's modulus between $E_0 = 0.25$ MPa to 4.0 MPa, spanning over the real $E_0 = 3.25$ MPa (26), while the results of Figs. 4–6 apply $E_0 = 1$ MPa.

Reference points are created in the middle of the top and bottom stiff square segments (yellow in Fig. 9*A*), which are rigidly coupled to all nodes on these square elements, with the boundary conditions visualized in white. The bottom reference nodes are restricted from moving in a vertical direction, and one is also constrained horizontally. The top reference nodes are homogeneously compressed vertically using displacement control. All nodes are free to rotate.

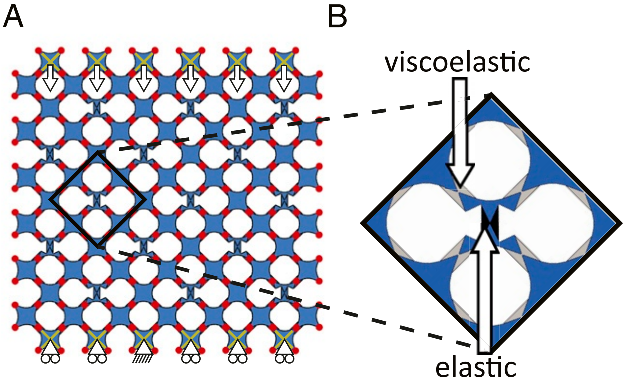

Fig. 9. Dynamic oligomodal finite element model: (*A*) modeled geometry with boundary conditions and nodes used for computing polarization with (*B*) enlarged supercell with material correspondence.

To prevent generating jerky stress waves, the load application follows a smooth step in the time domain, where the first and second derivatives of the displacement with respect to time are zero, with average strain rates between $\dot{\varepsilon} = 6.9 \cdot 10^{-7}\,\mathrm{s}^{-1}$ to $0.69\,\mathrm{s}^{-1}$.

After running the analyses, we compute the polarization of the holes, as defined in Fig. 5, by tracking the nodes corresponding to the points highlighted in red in Fig. 9*A*.

Data Availability. Experimental and numerical data (codes, raw images, and postprocessed images) have been deposited in Zenodo (https://doi.org/10.5281/zenodo.4699990) (42) .

ACKNOWLEDGMENTS. We thank D. Giesen and S. Koot for skillful technical assistance and S. Janbaz, R. van Mastrigt, D. Bonn, and M. van Hecke for insightful discussions. C.C. acknowledges funding from European Research Council Grant ERC-StG-Coulais-852587-Extr3Me.

1. K. Bertoldi, V. Vitelli, J. Christensen, M. van Hecke, Flexible mechanical metamaterials. *Nat. Rev. Mater.* **2**, 17066 (2017).
2. K. Bertoldi, P. Reis, S. Wilshaw, T. Mullin, Negative Poisson's ratio behavior induced by an elastic instability. *Adv. Mater.* **22**, 361–366 (2010).
3. J. Shim, C. Perdigou, E. Chen, K. Bertoldi, P. Reis, Buckling-induced encapsulation of structured elastic shells under pressure. *Proc. Natl. Acad. Sci. U.S.A.* **109**, 5978–5983 (2012).
4. C. Coulais, E. Teomy, K. de Reus, Y. Shokef, M. van Hecke, Combinatorial design of textured mechanical metamaterials. *Nature* **535**, 529–532 (2016).
5. C. Kane, T. Lubensky, Topological boundary modes in isostatic lattices. *Nat. Phys.* **10**, 39–45 (2014).
6. J. Paulose, B. Chen, V. Vitelli, Topological modes bound to dislocations in mechanical metamaterials. *Nat. Phys.* **11**, 153–156 (2015).
7. D. Rocklin, B. Chen, M. Falk, V. Vitelli, T. Lubensky, Mechanical Weyl modes in topological Maxwell lattices. *Phys. Rev. Lett.* **116**, 135503 (2016).
8. G. P. T. Choi, L. H. Dudte, L. Mahadevan, Programming shape using kirigami tessellations. *Nat. Mater.* **18**, 999–1004 (2019).
9. Y. Cho *et al.*, Engineering the shape and structure of materials by fractal cut. *Proc. Natl. Acad. Sci. U.S.A.* **111**, 17390–17395 (2014).
10. D. Liarte, O. Stenull, T. Lubensky, Multi-functional twisted-kagome lattices: Tuning by pruning mechanical metamaterials. *Phys. Rev. E* **101**, 063001 (2020).
11. P. Dieleman, N. Vasmel, S. Waitukaitis, M. van Hecke, Jigsaw puzzle design of pluripotent origami. *Nat. Phys.* **16**, 63–68 (2020).
12. A. Meeussen, E. Oguz, Y. Shokef, M. van Hecke, Topological defects produce exotic mechanics in complex metamaterials. *Nat. Phys.* **16**, 307–311 (2020).
13. J. Grima, K. Evans, Auxetic behavior from rotating squares. *J. Mat. Sci. Let.* **19**, 1563–1565 (2000).
14. T. C. Lubensky, C. L. Kane, X. Mao, A. Souslov, K. Sun, Phonons and elasticity in critically coordinated lattices. *Rep. Prog. Phys.* **78**, 073901 (2015).
15. S. D. Guest, J. W. Hutchinson, On the determinacy of repetitive structures. *J. Mech. Phys. Solid.* **51**, 383–391 (2003).
16. S. D. Papka, S. Kyriakides, In-plane crushing of a polycarbonate honeycomb. *Int. J. Solid. Struct.* **35**, 239–267 (1998).
17. S. Papka, S. Kyriakides, Experiments and full-scale numerical simulations of in-plane crushing of a honeycomb. *Acta Mater.* **46**, 2765–2776 (1998).
18. M. F. Ashby *et al.*, *Metal Foams: A Design Guide* (Butterworth-Heinemann, Woburn, MA, 2000).
19. V. Deshpande, N. Fleck, High strain rate compressive behaviour of aluminium alloy foams. *Int. J. Impact Eng.* **24**, 277–298 (2000).
20. W. Y. Jang, S. Kyriakides, On the crushing of aluminum open-cell foams: Part I. Experiments. *Int. J. Solid Struct.* **46**, 617–634 (2009).
21. S. Gaitanaros, S. Kyriakides, On the effect of relative density on the crushing and energy absorption of open-cell foams under impact. *Int. J. Impact Eng.* **82**, 3–13 (2015).
22. S. Gaitanaros, S. Kyriakides, A. M. Kraynik, On the crushing of polydisperse foams. *Eur. J. Mech. Solid.* **67**, 243–253 (2018).
23. J. Bernal, R. Fowler, A theory of water and ionic solution, with particular reference to hydrogen and hydroxyl ions. *J. Chem. Phys.* **1**, 515–548 (1933).
24. E. Lieb, Residual entropy of square ice. *Phys. Rev.* **162**, 162 (1967).
25. R. Baxter, Partition function of the eight-vertex lattice model. *Ann. Phys.* **70**, 193–228 (1972).
26. D. Dykstra, J. Busink, B. Ennis, C. Coulais, Viscoelastic snapping metamaterials. *J. Appl. Mech.* **86**, 111012 (2019).
27. M. Stern, V. Jayaram, A. Murugan, Shaping the topology of folding pathways in mechanical systems. *Nat. Commun.* **9**, 4303 (2018).
28. S. Janbaz, K. Narooei, T. van Manen, A. A. Zadpoor, Strain rate-dependent mechanical metamaterials. *Sci. Adv.* **6**, eaba0616 (2020).
29. H. Zhang, X. Guo, J. Wu, D. Fang, Y. Zhang, Soft mechanical metamaterials with unusual swelling behavior and tunable stress-strain curves. *Sci. Adv.* **4**, eaar8535 (2018).
30. S. M. Montgomery *et al.*, Magneto-mechanical metamaterials with widely tunable mechanical properties and acoustic bandgaps. *Adv. Funct. Mater.* **30**, 2005319 (2020).
31. T. Frenzel, M. Kadic, M. Wegener, Three-dimensional mechanical metamaterials with a twist. *Science* **358**, 1072–1074 (2017).
32. L. A. Shaw *et al.*, Computationally efficient design of directionally compliant metamaterials. *Nat. Commun.* **10**, 291 (2019).
33. M. A. Bessa, P. Glowacki, M. Houlder, Bayesian machine learning in metamaterial design: Fragile becomes supercompressible. *Adv. Mater.* **31**, 1904845 (2019).
34. E. Siefert, E. Reyssat, J. Bico, B. Roman, Bio-inspired pneumatic shape-morphing elastomers. *Nat. Mater.* **18**, 24–28 (2019).
35. T. Frenzel, C. Findeisen, M. Kadic, P. Gumbsch, M. Wegener, Tailored buckling microlattices as reusable light-weight shock absorbers. *Adv. Mater.* **28**, 5865–5870 (2016).
36. L. Jin *et al.*, Guided transition waves in multistable mechanical metamaterials. *Proc. Natl. Acad. Sci. U.S.A.* **117**, 2319–2325 (2020).
37. A. Zareei, B. Deng, K. Bertoldi, Harnessing transition waves to realize deployable structures. *Proc. Natl. Acad. Sci. U.S.A.* **117**, 4015–4020 (2020).
38. B. Pisanty, E. C. Oguz, C. Nisoli, Y. Shokef, Putting a spin on metamaterials: Mechanical incompatibility as magnetic frustration. arXiv [Preprint] (2021). https://arxiv.org/abs/2011.12867 (Accessed 6 May 2021).
39. C. Coulais, C. Kettenis, M. van Hecke, A characteristic length-scale causes anomalous size effects and boundary programmability in mechanical metamaterials. *Nat. Phys.* **14**, 40–44 (2018).
40. C. Coulais, A. Sabbadini, F. Vink, M. van Hecke, Multi-step self-guided pathways for shape-changing metamaterials. *Nature* **561**, 512–515 (2018).
41. Dassault Systèmes, Hyperelastic behavior of rubberlike materials. https://abaqus-docs.mit.edu/2017/English/SIMACAEMATRefMap/simamat-c-hyperelastic.htm. Accessed 7 January 2020.
42. A. Bossart, D. M. J. Dykstra, J. van der Laan, C. Coulais, Oligomodal metamaterials with multifunctional mechanics. Zenodo. https://doi.org/10.5281/zenodo.4699990. Deposited 19 April 2021.